Materials Advances

ROYAL SOCIETY OF CHEMISTRY

PAPER

View Article Online
View Journal | View Issue

Cite this: *Mater. Adv.*, 2025, 6, 2648

Epitaxial $PbZrO_3$ films from chemical solutions†

Alfredo Blázquez Martínez, ‡*[abc] Andreas Ost,[a] Goran Dražić, [de] Maja Koblar, [e] Andreja Benčan, [e] Torsten Granzow, [ac] Yves Fleming, [f] Alexander Ost, [bg] Emmanuel Defay, [abc] Mael Guennou [bc] and Sebastjan Glinšek *[ac]

Received 21st November 2024,
Accepted 19th March 2025

DOI: 10.1039/d4ma01155d

rsc.li/materials-advances

Lead zirconate ($PbZrO_3$) stands out as the prototypical antiferroelectric material, often studied for its applications in link capacitors and actuators. However, the conventional fabrication of single crystal films necessitates costly vacuum techniques and face scalability challenges. Exploiting scalable solution-based methods could unlock their full potential at reduced costs. Here, a chemical route for the preparation of high-quality single-crystal $PbZrO_3$ thin films on Nb-doped $SrTiO_3$ substrates is presented. Films with different thicknesses were grown and their structure was characterized by X-ray diffraction and transmission electron microscopy. Metal–insulator–metal capacitors were built to study their electrical switching characteristics. An unexpected ferroelectric-like switching is observed in 170 nm-thick film, while antiferroelectric-like switching is observed in 680 nm-thick films. The presence of ferroelectric-like switching is associated with the defect formation during the high-temperature annealing of the films.

1. Introduction

Antiferroelectrics (AFE) can be seen as materials where sublattices of electric dipoles can be identified at the microscopic scale that are aligned in opposite directions and cancel out, making them macroscopically non-polar.[1,2] In addition, at a critical electric field ($E_{AFE\rightarrow FE}$), a reversible electric-field-induced phase transition from the non-polar to a polar state takes place,[3] which is the most unique property of antiferroelectric materials and opens exciting applications for link capacitors,[4,5] electrocaloric cooling devices,[6] actuators[7] and electro-optic devices.[8,9] Among the available antiferroelectric materials, lead zirconate ($PbZrO_3$) is known as the prototypical system. Upon cooling down it undergoes a phase transition at around 510 K from a cubic paraelectric to an orthorhombic antiferroelectric phase where the Pb^{2+} ions are displaced along the $[100]_O$ direction of the orthorhombic unit cell.[10,11]

High-quality lead zirconate single crystal films can be grown by pulsed laser deposition[12–16] and metal organic chemical vapor deposition.[17] However, these techniques require expensive vacuum technologies and are not easily scalable.[18] On the other hand, chemical solution deposition processes are a low-cost, scalable alternative to manufacture functional thin films,[19,20] due to their compatibility with roll-to-roll processing,[21] direct patterning methods[22] and low-temperature processing.[23] Some reports can be found in the literature where high quality polycrystalline films are prepared using these methods.[24–26] However, the achievement of high quality single crystal films by solution deposition methods can be challenging due to the formation of grains, secondary phases, or defects during processing.

Here, a low-cost solution process for the fabrication of single crystal $PbZrO_3$ films on $SrTiO_3$ substrates is reported. A classical 2-methoxyethanol-based chemistry is used to prepare the precursor solution.[25] The films grow in $(120)_O$ and $(001)_O$ out-of-plane orthorhombic domains and are fully relaxed for all investigated thicknesses. Macroscopic electrical characterization studies show that 170 nm-thick films display ferroelectric-like switching, while 680 nm-thick films display antiferroelectric-like switching behaviour. The ferroelectric-like switching is explained by considering the formation of pinning defect complexes during the high-temperature annealing step, caused by sublimation of lead. Our results demonstrate the potential of solution deposition processes for the synthesis of single crystal thin $PbZrO_3$ films and highlight the role of defects on their behaviour.

[a] *Luxembourg Institute of Science and Technology, Smart Materials Unit, 41 rue du Brill, L-4422 Belvaux, Luxembourg. E-mail: sebastjan.glinsek@list.lu*
[b] *University of Luxembourg, Department of Physics and Materials Science, 41 rue du Brill, L-4422, Belvaux, Luxembourg*
[c] *Inter-Institutional Research Group Uni.lu-LIST on Ferroic Materials, 41 rue du Brill, L-4422 Belvaux, Luxembourg*
[d] *Department of Materials Chemistry, National Institute of Chemistry, Hajdrihova ulica 19, 1000 Ljubljana, Slovenia*
[e] *Jožef Stefan Institute, Electronic Ceramics Department, Jamova cesta 39, 1000 Ljubljana, Slovenia*
[f] *Luxembourg Institute of Science and Technology, Advanced Analyses and Support Unit, 41 rue du Brill, L-4422 Belvaux, Luxembourg*
[g] *Luxembourg Institute of Science and Technology, Scientific Instrumentation and Process Technology Unit, 41 rue du Brill, L-4420 Belvaux, Luxembourg*

† Electronic supplementary information (ESI) available. See DOI: https://doi.org/10.1039/d4ma01155d

‡ Present address: Helmholtz-Zentrum Berlin für Materialien und Energie GmbH, Hahn-Meitner Platz 1, 14109 Berlin, Germany.

2. Experimental

2.1. Thin-film fabrication

The $PbZrO_3$ precursor solution was synthesized from freeze-dried lead(II) acetate (99.99%, Merck) and a zirconium(IV) propoxide solution (70% in propanol, Merck). The precursors were dissolved in anhydrous 2-methoxyethanol (99.8%, Merck). Acetylacetone (99.5%, Merck) was used as a chelating agent. The mixture was refluxed for two hours under an argon atmosphere. The solution was then distilled and diluted with 2-methoxyethanol until it reached a concentration of 0.3 M. A Pb excess of 20% was used to compensate for PbO sublimation.

$PbZrO_3$ films were deposited by spin coating technique. (100)-oriented Nb-doped $SrTiO_3$ substrates (Crystal GmbH) were cleaned first in acetone, isopropanol, and then in water. Subsequently, the substrates were annealed at 400 °C for 10 minutes before deposition. The precursor solution was spin-coated at 3000 rpm for 30 seconds, followed by a drying step at 130 °C for 3 minutes and a pyrolysis step at 350 °C for 3 minutes. The films were crystallized in a rapid thermal annealing furnace (AS-Master, Annealsys) at 700 °C for 5 minutes in air. A thickness of 170 nm is obtained for each annealing cycle and thicker films were obtained by repeating those steps. $PbZrO_3$ thin films with a thickness of 170 nm, 340 nm, and 680 nm were prepared. To remove surface pyrochlore, a PbO capping layer was deposited on the top and crystallized at 700 °C. The remaining PbO crystals were removed (see Fig. S1, ESI†) with acetic acid (99.8%, Merck). To measure the ferroelectric properties, parallel plate capacitors were fabricated by lift-off photolithography and platinum sputtering.

2.2. Thin-film characterization

The crystal structure was analysed by X-ray diffraction (XRD) on a Bruker D8 diffractometer (Bruker, USA) in locked-couple configuration using Cu-Kα radiation. Lamella samples for scanning transmission electron microscopy (STEM) analyses were prepared with a focused ion-beam (FEI Nanolab Helios 650 – FIB). STEM studies were carried out using a probe Cs-corrected Jeol ARM 200 CF operated at 200 kV equipped with Centurio EDX system. The 4D-STEM dataset was acquired with a Merlin pixelated detector (Quantum Detectors, Oxford, UK). The center of mass and its derivatives were determined using a self-written Python code. Ferroelectric measurements were carried out at room temperature using a TF Analyzer 2000 (aixACCT, Germany). $P(E)$ loops were measured at a frequency of 100 Hz and a field amplitude of 1250 kV cm^{-1}. The measurement was performed by contacting two top electrodes to minimize the presence of imprint fields. This configuration is equivalent to measuring two capacitors in series with the conductive Nb-doped $SrTiO_3$ substrate acting as the common electrode between the two capacitors.

3. Results

3.1. Microstructure analysis

$\theta-2\theta$ XRD patterns (Fig. 1(a)) reveal the perfect $(001)_{pc}$ orientation of $PbZrO_3$ films and the absence of pyrochlore peaks at all thicknesses. The $(002)_{pc}$ peak of the film (Fig. 1(b)) is split into two peaks corresponding to the expected $(240)_O$ and $(004)_O$ orthorhombic reflections. Their positions match well the theoretical positions of the orthorhombic Pbam phase. Besides, the peaks do not shift with increasing thickness, indicating that there is no significant stress relaxation with increasing thickness. In order to check the in-plane orientation, ϕ-scans were carried out for the $(110)_O$ and $(042)_O$ oblique reflections of the film and the $(101)_C$ reflection of the $SrTiO_3$ substrate (Fig. 1(c)). All ϕ-scans show a 4-fold symmetry. The $(110)_O$ of the films are found at the same ϕ-angle as the substrate $(101)_C$ and reveal the presence of the 4 domain variants expected with a $(120)_O$ direction out of plane (see Fig. S2 for the detailed depiction of the orientations of all possible ferroelastic domains, ESI†). The $(042)_O$ reflections – corresponding to pseudo-cubic $(111)_{pc}$ – are observed, as expected, at ϕ-angles shifted by 45° with respect to the $(101)_C$ substrate peaks. Overall, this demonstrates a single crystal, multidomain state with the presence of all 6 possible ferroelastic domain variants. The presence of all variants suggests that the film is not under any anisotropic stress high enough to create a preference for any particular domain orientation when the film is cooled down from the cubic phase at the crystallization temperature of 700 °C to below T_C.

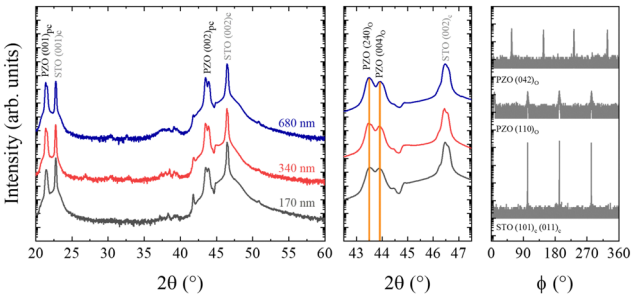

Fig. 1 X-ray diffraction (XRD) analysis of the films. (a) $\theta-2\theta$ patterns of the $PbZrO_3$ films with different thicknesses. (b) Detailed view around the $(240)_O$ and $(004)_O$ $PbZrO_3$ peaks (vertical lines denote their position according to PDF file No. 01-089-1296. All non-marked peaks correspond to the substrate. (c) ϕ-scans of the 170 nm-thick film.

Detailed microstructure was analysed using STEM. High-angle annular dark-field (HAADF) and bright-field (BF) STEM micrographs (Fig. 2(a) and (b)) of the 170 nm-thick films reveal a dense film with some pores present at the interface between the film and the substrate (see circles in Fig. 2(b)). A nano-grained layer of approximately 10 nm is present at the top surface. It is revealed to be Pb-deficient by energy-dispersive X-ray spectroscopy (EDXS) (see Fig. S3, ESI†), pointing towards the presence of a surface secondary phase. Additionally, a gradient of the Pb/Zr ratio, with more Pb at the film/substrate interface, is observed. Both are typical features of solution-deposited Pb-based perovskites.[27] The shaded areas indicate the formation of different ferroelastic domains formed as the film is cooled down below T_C after crystallisation. Fig. 2(c) shows the selected area diffraction (SAED) of the area shown in the miniature. It indicates that the $PbZrO_3$ is a single crystal, oriented towards the $[100]_{pc}$ direction, which corresponds to the $[120]_O$ and $[002]_O$ orientations in the orthorhombic notation. $\frac{1}{4}$ superlattice spots from an antiferroelectric domain

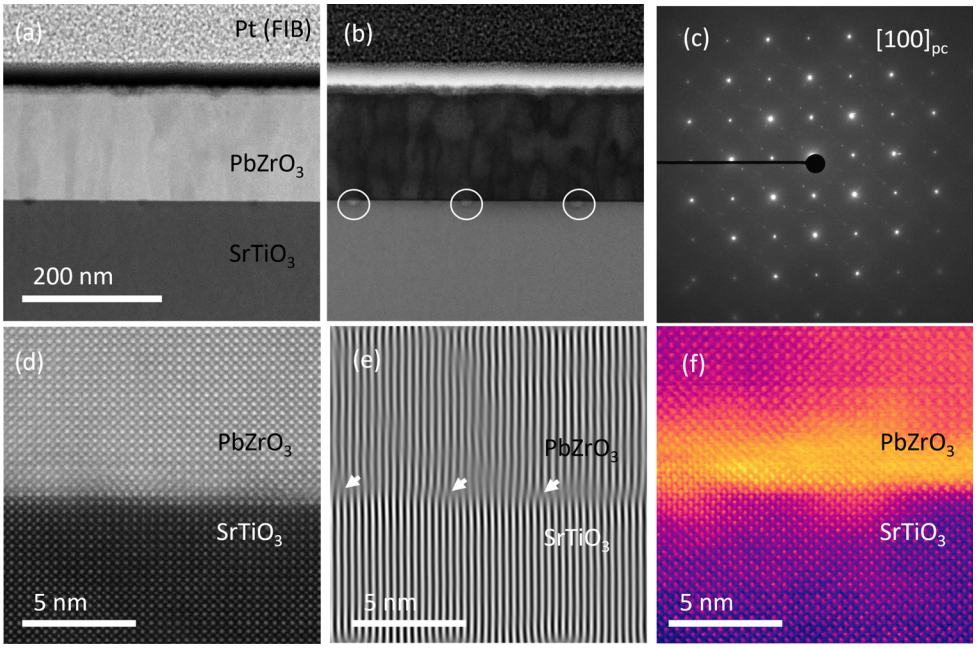

Fig. 2 Scanning transmission electron microscopy (STEM) images of 170 nm-thick film. High-angle annular dark-field (HAADF) (a) and bright-field (BF) (b) STEM micrographs of 170 nm-thick film. White circles in (b) highlight pores. (c) Selected area diffraction pattern (SAED) of the $PbZrO_3$ film in $[100]_{pc}$ zone axis showing $\frac{1}{4}$ superlattice spots in ⟨110⟩ directions. (d) High resolution HAADF micrograph of the film/substrate interface with corresponding (e) Inverse filtered fast Fourier transform (i-FFT) image with marked dislocations and (f) Virtual low-angle-dark-field image of the film/substrate interface created from a 4D-STEM dataset where higher contrast represent higher local strain at the film/substrate interface.

structure are also observed. A closer look at the interface quality is shown in Fig. 2(d). The HAADF TEM micrograph shows an atomically flat interface. At the film/substrate interface, a greater number of dislocations can be observed (Fig. 2(e)), that lead to a full relaxation of epitaxial strains within the first 5 nm of the film, as shown in Fig. 2(f). This agrees with the absence of strain seen in XRD diffractograms.

The detailed microstructure of the 680 nm-thick films is shown in Fig. 3. The BF and HAADF STEM micrographs in Fig. 3(a) and (b) reveal dense films with some pores present at the interface between layers. A gradient in the Pb/Zr ratio can be observed in Fig. 3(c), displaying a Zr-rich and Pb-deficient interface between the successive layers. The four layers, corresponding to each crystallization step, can be identified. The SAED patterns in Fig. 3(d) reveal $\frac{1}{4}$ superlattice spots in the $[110]_{pc}$ directions, which reveals both the antiparallel displacements of Pb and domain coexistence, as previously observed.[3,28]

3.2. Electrical properties

Fig. 4 shows polarization–electric field ($P(E)$) loops as well as the corresponding loops of current density ($j(E)$) for the films with thicknesses between 170 nm and 680 nm. The absence of notable leakage current even at high field indicates the high quality of the films. Complex switching curves were observed for all samples, with $j(E)$ displaying multiple peaks indicating poling and depoling processes.

For the 170 nm thick film, there appears to be two main peaks for both positive and negative electric fields at

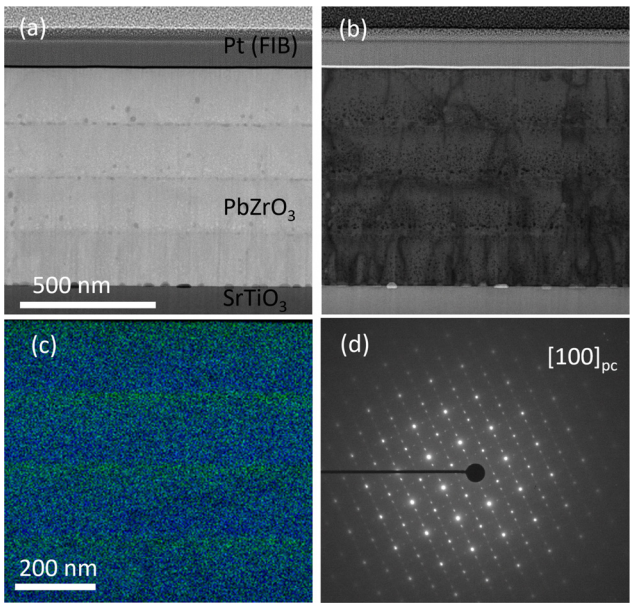

Fig. 3 STEM images of a 680 nm-thick film. High-angle annular dark-field (HAADF) (a) and bright-field (BF) (b) STEM micrographs of 680 nm-thick film. (c) Composite EDXS image of $PbZrO_3$ film using Zr K (green) and Pb M lines (blue). (d) Selected area diffraction pattern (SAED) of the $PbZrO_3$ film in $[100]_{pc}$ zone axis showing $\frac{1}{4}$ superlattice spots in ⟨110⟩ directions.

950 kV cm^{-1} and partial back-switching with decreasing field at 200 kV cm^{-1}. The exact field is difficult to determine because of the breadth of the peak. Two more peaks are observed at 300 kV cm^{-1} with increasing field, but appear only weakly.

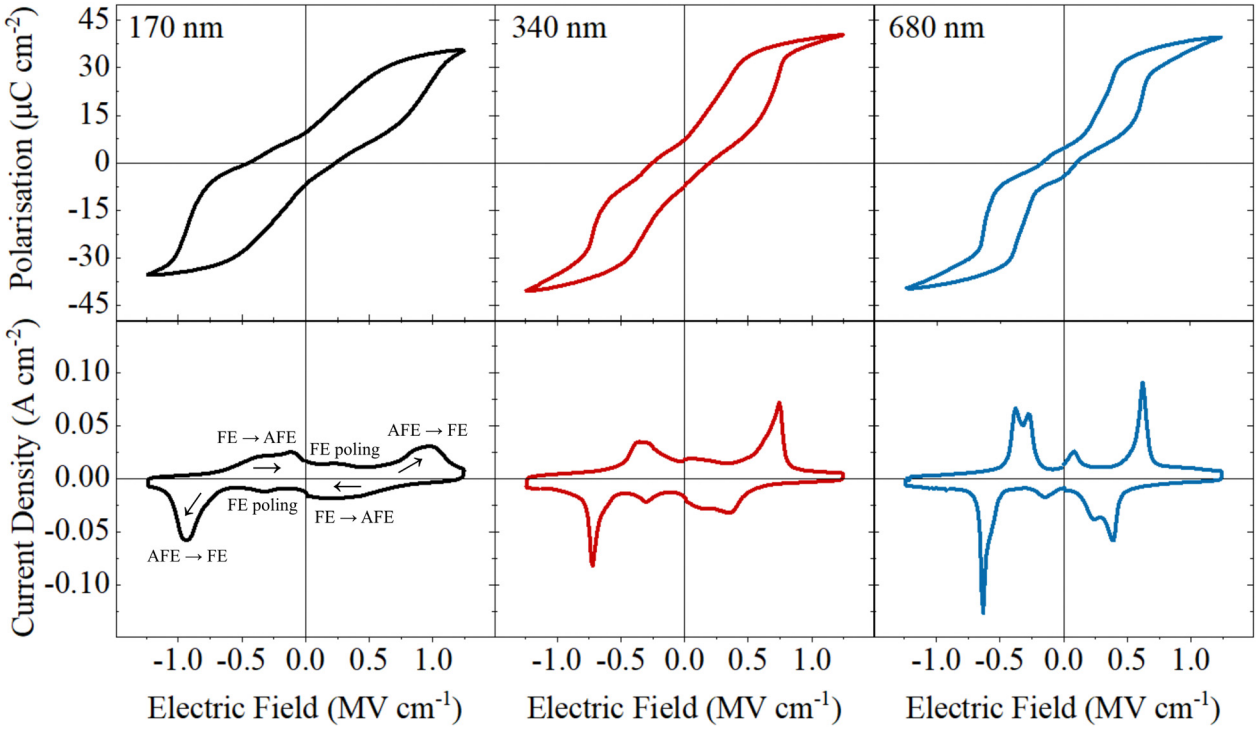

Fig. 4 $P(E)$ and $j(E)$ loops of the $PbZrO_3$ films with different thicknesses. The measurements were performed at 100 Hz.

With increasing film thickness, the peaks become more pronounced, in agreement with the increasing antiferroelectric nature of the films. For the 340 nm thick films, the $E_{AFE\rightarrow FE}$ decreases to 744 kV cm^{-1} and the $E_{FE\rightarrow AFE}$ increases to 365 kV cm^{-1}.

The $P(E)$ loop for the 680 nm thick film most closely resembles that expected for an antiferroelectric, with an antiferroelectric–ferroelectric transition field $E_{AFE\rightarrow FE}$, defined by the maximum of the poling current, of 620 kV cm^{-1} and the reverse process occurring when the field drops again below $E_{FE\rightarrow AFE}$ at 380 kV cm^{-1}. These peaks are interpreted as indicating the build-up of polarization during the field-induced transition of the AFE part of the films to a FE phase (620 kV cm^{-1}) and the return to the AFE phase after field removal (380 kV cm^{-1}). The peak splitting in the AFE → FE transition indicate that different regions of the film transition at slightly different electric fields. This may arise from dissimilar domain nucleation and growth energies at the different electrode/antiferroelectric interfaces.[29]

Ferroelectric switching is evident even in the 680 nm thick film, as indicated by the peaks in the $j(E)$ loops below 200 kV cm^{-1}, resulting in a remanent polarization of P_r = 4.7 μC cm^{-2}. The continued existence of the peaks assigned to the switching of FE domains indicates that the film is still a mixture of both AFE and FE phase contents.

A transition from an antiferroelectric-like behavior to a more ferroelectric-like behavior is also observed upon repetitive cycling of the capacitor. This is shown on the example of the $P(E)$ and $j(E)$ loops of the 340 nm thick film in Fig. 5. The sample is cycled at a frequency of 100 Hz and an amplitude of 1250 kV cm^{-1}. After a preset cycle number, cycling is interrupted and a hysteresis measurement is taken. As already seen in Fig. 4, the first hysteresis curve shows a mostly antiferroelectric behavior, but still has a low but non-zero remanent polarization indicative of ferroelectric contributions to the hysteresis. Upon cycling, the antiferroelectric-like loops transform into ferroelectric-like shaped loops: the clear maxima of the current density indicating the poling/depoling processes merge into a single broad maximum indicating ferroelectric domain reversal, and the remanent polarization increases until a stable state is reached after less than 500 cycles.

4. Discussion

The high quality and epitaxial nature of the $PbZrO_3$ films synthesized by a low-cost solution deposition method is demonstrated by the structural, microstructural, and electrical characterization. The complex switching curves, with $j(E)$ displaying multiple peaks that indicate poling and depoling processes, together with the presence of 1/4 superlattice spots indicate the presence of AFE domains in all films. Note that the stronger AFE character of the thicker films cannot be directly correlated with the intensity of the 1/4 superlattice reflections along the ⟨110⟩ directions, as the diffraction pattern intensity can be influenced by the TEM sample thickness and domain orientation within the analyzed area. The unexpected appearance of ferroelectric-like characteristics in the 170 nm-thick film, the gradual transition to more antiferroelectric-like behavior with increasing thickness, and the transition from an

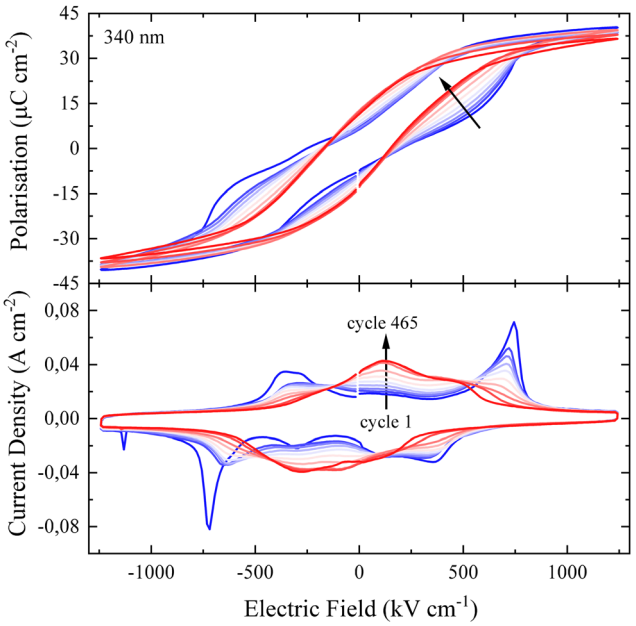

Fig. 5 $P(E)$ and $j(E)$ loops of a 340 nm-thick film after different number of cycles.

antiferroelectric-like behavior to a more ferroelectric-like behavior upon repetitive electrical cycling for the thicker films require closer analysis.

Several mechanisms that can induce ferroelectricity in antiferroelectric materials have been proposed in literature. First, there is the emergence and stabilization of ferroelectric or even ferrielectric phases through epitaxial strain as reported by Chaudhuri *et al.*[14] and Liu *et al.*[30] This, however, is rather observed in ultrathin films at critical thicknesses below 20 nm, which is an order of magnitude below the thicknesses reported here. Besides, as revealed by TEM, the strain in our films is relaxed within the first few nanometers and the positions of the XRD peaks do not shift with thickness, also indicating identical strain states in all the films. We also note that the appearance of new polar phases by epitaxial strain have been shown to cause a small remanent polarization in the double-hysteresis loop and do not induce a full transition from antiferroelectric-like to ferroelectric-like hysteresis loops. Therefore, this mechanism is discarded as an explanation for the present results.

A more plausible scenario is a transition driven by the formation of structural defects that interact with the antiferroelectric-to-ferroelectric phase boundaries. Pan *et al.*[31] observed similar electrical characteristics in their $PbZrO_3$ deposited by pulsed laser deposition using different O_2 partial pressures, and therefore creating films with different point defect concentrations. Their films deposited with low O_2 partial pressure exhibit similar transitions from antiferroelectric-like to ferroelectric-like hysteresis loops, both under high electric fields as well as under repetitive cycling, highlighting the role of defect formation in the hysteresis characteristics.

In the present case, the variation of oxygen vacancy concentration results from the high-temperature processing. During annealing of the amorphous films at 700 °C, PbO is prone to sublimation. As crystallization proceeds from the $SrTiO_3$/$PbZrO_3$ interface, this leads to a compositional gradient of the Pb/Zr ratio through the thickness of the films, as evidenced by the EDXS measurements. Pb vacancies are formed and compensated by the creation of oxygen vacancies or the change of valence state of the cations. If the off-stoichiometry becomes too severe, a pyrochlore phase is stabilized. Indeed, TEM reveals Zr-rich secondary phase on the surface, which could be pyrochlore. The oxygen vacancies result in a stabilization of the ferroelectric phase against the antiferroelectric phase. As the films grow thicker, the specific surface, and with it the influence of Pb sublimation, is decreased, so the films approach the antiferroelectric behavior expected for $PbZrO_3$ in the bulk limit.

This leaves the question why the ferroelectric character increases with cycling. As this phenomenon is already observed within the first few cycles, diffusion or drift of the ionic defects can be excluded as a possible cause. We propose a hypothesis based on the existing defects hindering the AFE → FE transition during field decrease. During the first loop, the fraction of sample volume in the antiferroelectric phase is still relatively large, and as a consequence the character of the hysteresis is still largely antiferroelectric. With each field excursion, some of this volume is switched to the ferroelectric phase and prevented to return to the antiferroelectric phase by the defects; as a result, the ferroelectric character increases with each cycle, until practically the entire volume is ferroelectric.

5. Conclusion

In summary, a method to prepare epitaxial single crystal $PbZrO_3$ films by solution deposition is described. Epitaxial strain is relaxed due to the formation of dislocation in the first 5 nm of the films. The films with a thickness of 680 nm display antiferroelectric switching properties. However, an unexpected ferroelectric-like switching is observed as the film thickness is reduced and is even dominant in the 170 nm films. This behaviour is associated with defect formation during the high-temperature annealing of the films, *e.g.*, lead gradients within the film, whereby pinning defects prevent the back-switching, *i.e.* the antiferroelectric-to-ferroelectric phase transition. Thicker films minimize the impact of lead-deficiency gradients and the defect-induced stabilization of ferroelectric domains. The control of these defects, both by controlling the stoichiometry during film synthesis or later by electrical cycling opens the opportunity to manipulate the switching properties of antiferroelectric $PbZrO_3$.

Data availability

The raw data generated in this study have been deposited in the Zenodo repository under DOI: **10.5281/zenodo.15084379**.

Conflicts of interest

There are no conflicts to declare.

Acknowledgements

ABM, SG and TG acknowledge financial support from the Luxembourgish National Research Fund (FNR) under the project PACE (Photovoltaics: Advanced Concepts for high Efficiency, PRIDE17/12246511/PACE). AO acnowledges financial support from the Luxembourgish National Research Fund (FNR) under the project/INTER/DFG/17/11779689. AO and SG acknowledge financial support from the Luxembourgish National Research Fund (FNR) under the project FLASHPOX (C21/MS/16215707). AB, MK and GD would like to thank the Slovenian Research and Innovation Agency for funding (J7-4637, J2-3041).

Notes and references

1 C. Kittel, *Introduction to Solid State Physics*, Wiley, 2004.
2 G. Shirane, E. Sawaguchi and Y. Takagi, *Phys. Rev.*, 1951, **84**, 476–481.
3 C. A. Randall, Z. Fan, I. Reaney, L. Chen and S. Trolier-McKinstry, *J. Am. Ceram. Soc.*, 2021, **104**, 3775–3810.
4 Z. Liu, T. Lu, J. Ye, G. Wang, X. Dong, R. Withers and Y. Liu, *Adv. Mater. Technol.*, 2018, **3**, 1–21.
5 P. Gao, C. Liu, Z. Liu, H. Wan, Y. Yuan, H. Li, Y. Pu and Z.-G. Ye, *J. Eur. Ceram. Soc.*, 2022, **42**, 1370–1379.
6 P. Vales-Castro, R. Faye, M. Vellvehi, Y. Nouchokgwe, X. Perpiñà, J. M. Caicedo, X. Jordà, K. Roleder, D. Kajewski, A. Perez-Tomas, E. Defay and G. Catalan, *Phys. Rev. B*, 2021, **103**, 054112.
7 K. Uchiho, *Mater. Res. Innovations*, 1997, **1**, 163–168.
8 F. Wang, K. K. Li and G. H. Haertling, *Opt. Lett.*, 1992, **17**, 1122.
9 P. P. Biswas, C. Milesi-Brault, A. Blázquez Martínez, N. Aruchamy, L. Song, V. Kovacova, S. Glinšek, T. Granzow, E. Defay and M. Guennou, *Phys. Rev. Mater.*, 2022, **6**, 1–7.
10 J. Zhai and H. Chen, *Appl. Phys. Lett.*, 2003, **82**, 2673–2675.
11 Y. Liu, R. Niu, A. Majchrowski, K. Roleder, K. Cordero-Edwards, J. M. Cairney, J. Arbiol and G. Catalan, *Phys. Rev. Lett.*, 2023, **130**, 216801.
12 K. Boldyreva, D. Bao, G. Le Rhun, L. Pintilie, M. Alexe and D. Hesse, *J. Appl. Phys.*, 2007, **102**, 044111.
13 L. Pintilie, K. Boldyreva, M. Alexe and D. Hesse, *J. Appl. Phys.*, 2008, **103**, 024101.
14 A. Roy Chaudhuri, M. Arredondo, A. Hähnel, A. Morelli, M. Becker, M. Alexe and I. Vrejoiu, *Phys. Rev. B*, 2011, **84**, 1–8.
15 P. Dufour, T. Maroutian, M. Vallet, K. Patel, A. Chanthbouala, C. Jacquemont, L. Yedra, V. Humbert, F. Godel, B. Xu, S. Prosandeev, L. Bellaiche, M. Otoničar, S. Fusil, B. Dkhil and V. Garcia, *Appl. Phys. Rev.*, 2023, **10**, 021405.
16 H. Pan, M. Zhu, E. Banyas, L. Alaerts, M. Acharya, H. Zhang, J. Kim, X. Chen, X. Huang and M. Xu, *et al.*, *Nat. Mater.*, 2024, 1–7.
17 M. P. Moret, J. J. Schermer, F. D. Tichelaar, E. Aret and P. R. Hageman, *J. Appl. Phys.*, 2002, **92**, 3947–3957.
18 D. H. A. Blank, M. Dekkers and G. Rijnders, *J. Phys. D: Appl. Phys.*, 2014, **47**, 034006.
19 P. Muralt, *J. Micromech. Microeng.*, 2000, **10**, 136–146.
20 G. L. Brennecka, J. F. Ihlefeld, J. P. Maria, B. A. Tuttle and P. G. Clem, *J. Am. Ceram. Soc.*, 2010, **93**, 3935–3954.
21 D. Angmo, T. T. Larsenâe-Olsen, M. Jørgensen, R. R. Søndergaard and F. C. Krebs, *Adv. Energy Mater.*, 2013, **3**, 172–175.
22 S. Glinšek, L. Song, V. Kovacova, M. A. Mahjoub, N. Godard, S. Girod, J. Biagi, R. Quintana, T. Schleeh, M. Guedra, M. Rupin and E. Defay, *Adv. Mater. Technol.*, 2022, **7**, 1–7.
23 L. Song, J. Cardoletti, A. Blázquez Martínez, A. Benčan, B. Kmet, S. Girod, E. Defay and S. Glinšek, *Nat. Commun.*, 2024, **15**, 1890.
24 T. Sa, N. Qin, G. Yang and D. Bao, *Appl. Phys. Lett.*, 2013, **102**, 172906.
25 C. Milesi-Brault, N. Godard, S. Girod, Y. Fleming, B. El Adib, N. Valle, S. Glinšek, E. Defay and M. Guennou, *Appl. Phys. Lett.*, 2021, **118**, 042901.
26 Y. Yao, A. Naden, M. Tian, S. Lisenkov, Z. Beller, A. Kumar, J. Kacher, I. Ponomareva and N. Bassiri-Gharb, *Adv. Mater.*, 2023, **35**, 2206541.
27 F. Calame and P. Muralt, *Appl. Phys. Lett.*, 2007, **90**, 062907.
28 Z. Li, Z. Fu, H. Cai, T. Hu, Z. Yu, Y. Luo, L. Zhang, H. Yao, X. Chen, S. Zhang, G. Wang, X. Dong and F. Xu, Discovery of electric devil's staircase in perovskite antiferroelectric, 2022, DOI: **10.1126/sciadv.abl9088**.
29 P. Gao, C. T. Nelson, J. R. Jokisaari, S.-H. Baek, C. W. Bark, Y. Zhang, E. Wang, D. G. Schlom, C.-B. Eom and X. Pan, *Nat. Commun.*, 2011, **2**, 591.
30 Y. Liu, R. Niu, R. Uriach, D. Pesquera, J. M. C. Roque, J. Santiso, J. M. Cairney, X. Liao, J. Arbiol and G. Catalan, *Microstructures*, 2024, **4**, 2024045.
31 H. Pan, Z. Tian, M. Acharya, X. Huang, P. Kavle, H. Zhang, L. Wu, D. Chen, J. Carroll, R. Scales, C. J. G. Meyers, K. Coleman, B. Hanrahan, J. E. Spanier and L. W. Martin, *Adv. Mater.*, 2023, **35**, 1–9.